Check for updates

Near-infrared Ternary Tandem Solar Cells

Yongxi Li,[a] Jiu-Dong Lin,[b] Xiao Liu,[a] Yue Qu,[a] Fu-Peng Wu,[b] Feng Liu,[c] Zuo-Quan Jiang,[b] Stephen R. Forrest,[a]*

[a]Department of Electrical Engineering and Computer Science, University of Michigan, Ann Arbor, Michigan 48109, USA.

[b]Institute of Functional Nano & Soft Materials (FUNSOM), Soochow University, Suzhou, Jiangsu 215123, P.R. China.

[c]Department of Physics and Astronomy, and Collaborative Innovation Center of IFSA (CICIFSA), Shanghai Jiaotong University, Shanghai 200240, P. R. China.

[*]*email: steveforr@umich.edu*

Author Manuscript

ABSTRACT

The paucity of near-infrared (NIR) organic materials with high absorption at long wavelengths combined with large diffusion lengths and charge mobilities, has been an impediment to progress in achieving high efficiency organic tandem solar cells. Here we employ a subcell within a series tandem stack that comprises a solution-processed ternary blend of two NIR-absorbing non-fullerene acceptors, and a polymer donor combined with a small molecular weight, short wavelength fullerene-based subcell grown by vacuum thermal evaporation. The ternary cell achieves a power conversion efficiency of 12.6 ± 0.3% with a short circuit current of 25.5 ± 0.3 mA cm^{-2}, open circuit voltage of 0.69 ± 0.01 V and a fill factor of 0.71 ± 0.01 under 1 sun, AM 1.5G spectral illumination. The success of this device is a result of the nearly identical offset energies between the lowest unoccupied molecular orbitals (MOs) of the donors with the highest occupied MO of the acceptor, resulting in a high open circuit voltage. An anti-reflection coated tandem structure combining these subcells demonstrates a power conversion efficiency of 15.4±0.3%.

This is the author manuscript accepted for publication and has undergone full peer review but has not been through the copyediting, typesetting, pagination and proofreading process, which may lead to differences between this version and the Version of Record. Please cite this article as doi: 10.1002/adma.201804416.

This article is protected by copyright. All rights reserved.

I. INTRODUCTION

Organic photovoltaics (OPVs), have the potential for producing low-cost and ubiquitous renewable energy in the future, due to their reliance on abundant and environmentally friendly carbon-based materials. Furthermore, their ability to be deposited on flexible, light weight and transparent substrates provides a path to mass production via continuous roll-to-roll deposition[1]. By stacking both large and small energy-gap cells into a tandem OPV, the efficiency can be improved by minimizing the thermalization losses[2-5]. However, the relative lack of high performance, small-energy gap cells has impeded the progress in tandem solar cell efficiency[6-9]. Recently, our group demonstrated an organic tandem solar cell with a power conversion efficiency as high as *PCE* = 15.0% under 1 sun, AM 1.5G spectral illumination[10]. This result was based on the combination of a fullerene based cell deposited via vacuum thermal evaporation (VTE), along with a solution-processed, two-component NIR non-fullerene acceptor (NFA) subcell absorbing between wavelengths of 650 – 850 nm with *PCE* ~ 11%[11].

Although recent rapid developments of small energy gap NFAs provides opportunities to achieve high efficiency NIR cells, only a few non-fullerene acceptors have significant absorption and wavelengths greater than 1000 nm[12-16]. The successful design of narrow energy gap NFAs requires precise tuning of the energy levels while maintaining a sufficient heterojunction energy offset to efficiently drive the dissociation of excitons. In this context, ternary blend OPVs containing one additional electron donor or acceptor material are a promising way to overcome the efficiency bottleneck encountered by conventional binary cells[17-22]. In this work, we use ternary blends of two NIR non-fullerene acceptors with a polymer donor to significantly reduce energy losses. A narrow energy gap non-fullerene acceptor, TT-FIC (4,4,10,10-tetrakis(4-hexylphenyl)-4,10-dihydrothieno [2",3":4',5']thieno[3',2':4,5] cyclopenta[1,2-b]thieno[2,3-d]thiophene-2,8-diyl)bis(2-(3-oxo-

This article is protected by copyright. All rights reserved.

Author Manuscript

2,3-dihydroinden-5,6-difluoro-1-ylidene) malononitrile)[13] sharing similar lowest unoccupied molecular orbital (LUMO) energies with a second acceptor BT-CIC, (absorption up to 1000 nm) is blended with the polymer PCE-10 (poly[4,8-bis(5-(2-ethylhexyl)thiophen-2-yl)benzo[1,2-b:4,5-b']dithiophene-co-3-fluorothieno[3,4-b]thio-phene-2-carboxylate]). The resulting small differences in offset energies (40 meV) between the LUMOs of the acceptors and the highest occupied molecular orbitals (HOMOs) of the donors, along with the significantly different energy gaps (by 0.11 eV) of the acceptors, result in an open circuit voltage (V_{OC}) that is close to the maximum possible for this narrow energy gap system.

The *PCE* of the ternary cell is increased from 10.8±0.2% in a BT-CIC:PCE-10 cell to 12.6±0.3% in the BT-CIC:TT-FIC:PCE-10 ternary OPV. Furthermore, the short-circuit current density (J_{SC}) is increased from 22.3±0.4 mA cm^{-2} to 25.5±0.3 mA cm^{-2}. Importantly, the absorption of the ternary cell is extended to 1000 nm with the energy loss ($E_{loss} = E_g - qV_{OC}$ where E_g is the smaller energy gap of either the donor or acceptor) decreased from 0.64 to 0.55 eV.

Although the *PCE* of ternary single-junction solar cells exceeds 12%, their light absorption remains limited by the very thin active layer (~100 nm) due to the low charge carrier mobility of the organic semiconductors. While energy conversion can be improved with a multi-junction architecture, the potential of ternary subcells in multi-junction devices has not yet been substantially explored[17]. Here, we demonstrate an anti-reflection-coated (ARC) tandem structure combining both binary- and ternary-based OPVs, reaching *PCE* = 15.4±0.3% under 1 sun, AM 1.5G simulated illumination (area = 2mm^2). This suggests the potential for the use of ternary subcells in multijunction devices that can achieve even higher efficiencies than reported here.

II. RESULTS

This article is protected by copyright. All rights reserved.

Author Manuscript

The chemical structures of the PCE-10, BT-CIC and TT-FIC are shown in **Figure 1a**. The synthetic route for TT-FIC is shown in **Scheme S1** in the Supplementary Information (SI). All materials are soluble in chloroform (CF), chlorobenzene (CB), and *ortho*-dichlorobenzene (*o*-DCB). Thin film absorption spectra of PCE-10, BT-CIC and TT-FIC are shown in **Figure 1b**. In contrast to BT-CIC, the absorption spectrum of TT-FIC is red-shifted by 50 nm, resulting in absorption between λ = 600 nm and 1000 nm and a small optical energy gap of 1.24 eV. The absorption of blended films with different weight ratios of TT-FIC are shown in **Figure 1c**. With increasing TT-FIC content, the absorption between 600 and 1000 nm in the ternary blends gradually increases due to the change in NIR absorption by the addition of TT-FIC.

Cyclic voltammetry in **Figure S1** gives the HOMO (E_{HOMO}) and LUMO (E_{LUMO}) energies of -5.42 (±0.02) and -4.13 (±0.02) eV, respectively, for TT-FIC, and -5.49 (±0.02) and −4.09 (±0.02) eV for BT-CIC. TT-FIC shows a lower HOMO-LUMO energy gap (1.29 eV) than BT-IC (1.40 eV, see **Figure 1d**), which is consistent with optical measurements. However, TT-FIC exhibits shallower HOMO and deeper LUMO energies compared with BT-CIC, which leads to a reduction of V_{OC} in TT-FIC based binary OPVs.

The morphologies of both the binary and ternary blends were characterized by grazing incidence x-ray diffraction. As shown in **Figure S2**, the two binary blends show quite different solid-state ordering. The PCE-10:BT-CIC blends show more intense diffraction features with contributions from both PCE-10 and BT-CIC compared to PCE-10:TT-FIC. This indicates that the crystallization of both PCE-10 and TT-FIC is decreased in the blends. In ternary blends, both PCE-10:BT-CIC:TT-FIC (1:1.25:0.25, w/w/w) and PCE-10:BT-CIC:TT-FIC (1:1.25:0.5, w/w/w) showed similar structural ordering compared to PCE-10:BT-CIC (1:1.5, w/w), but further increasing the content of TT-FIC to 0.75 caused only a small decrease in diffraction peak intensity. This suggest that PCE-10 and BT-CIC are

This article is protected by copyright. All rights reserved.

Author Manuscript

guiding the morphology of the ternary mixture. The TT-FIC molecules locate between PCE-10 and BT-CIC domains while leaving the size and structure of the PCE-10 and BT-CIC domains unchanged. Therefore, electron transport and collection occur through the BT-CIC instead of TT-FIC. Thus, the TT-FIC functions as a sensitizer. This is one possible reason that the addition of TT-FIC to PCE10: BT-CIC does not influence V_{OC} (see below).

Phase segregation within the blends was further studied by resonant soft x-ray diffraction, with results in **Figure S2c**. Both of the PCE-10:BT-IC (1:1.5, w/w) and PCE-10:TT-FIC (1:1.5, w/w) blends show a multi-length scaled morphology, with one peak at Q = 0.085 $Å^{-1}$ (corresponding to a distance of 74 nm) and another at 0.025 $Å^{-1}$ (250 nm), suggesting structure at a dimension of hundreds of nanometers. In contrast, a single diffraction peak was observed in all three ternary blends, where PCE-10:BT-CIC:TT-FIC (1:1.25:0.5, w/w/w) exhibits the smallest scale for phase separation (74 nm) compared to the PCE-10:BT-CIC:TT-FIC (1:1.25:0.25, w/w/w, 94 nm) and PCE-10:BT-CIC:TT-FIC (1:1.25:0.75, w/w/w, 106 nm). The PCE-10:BT-CIC:TT-FIC blend film shows a high intensity peak at 0.067 A^{-1} (corresponding to a distance of 94 nm) in **Figure S2**, while the PCE-10:BT-CIC:TT-FIC blend with a lower intensity peak at 0.085 A^{-1} (corresponding to a distance of 74 nm). The higher intensity indicates greater domain purity, but the enlarged phase separation for PCE-10:BT-CIC:TT-FIC blend is inferior for charge extraction. Therefore, it is hard to predict the J_{SC} only from the morphology study.

Atomic force microscopy (AFM) images of binary and ternary blends are shown in **Figure S3**, PCE-10:BT-CIC:TT-FIC (1:1.25:0.5, w/w/w) blend with a root-mean-square roughness of 0.79 nm, compared with 1.15 nm for the PCE-10:BT-CIC:TT-FIC (1:1.25:0.25, w/w/w) and 0.91 nm for PCE-10:BT-CIC:TT-FIC (1:1.25:0.75, w/w/w) blends.

Ternary OPVs were fabricated with the device structure: indium tin oxide (ITO)/ poly(3,4-ethylenedioxythiophene)-poly(styrenesulfonate) (PEDOT:PSS) (50 nm) /PCE-

This article is protected by copyright. All rights reserved.

Author Manuscript

10:BT-CIC:TT-FIC (1:1.25:*x*, 95 nm)/1,3,5-tri(m-pyridin-3-ylphenyl)benzene (TmPyPB) (5 nm)/Ag (100 nm). To systematically study the effects of the blend ratios, we also prepared a binary cell with the structure: ITO/PEDOT:PSS (50 nm) /PCE-10: TT-FIC (1:1.5, 100 nm) /ZnO (35 nm) /Ag(100 nm). The ZnO nanoparticles were used for the electron transporting layer to improve the contact between TmPyPB and PCE-10:TTFIC. Details of fabrication are found in Methods.

The current-density-voltage ($J-V$) characteristics of PCE-10:BT-CIC:TT-FIC (1:x:y) blends are plotted in **Figure 2a**, with a summary of device performance in **Table 1**. Compared to the BT-CIC, the TT-FIC-based binary device shows increased J_{SC} (24.7±0.6 mA cm^{-2} vs. 22.3±0.4 mA cm^{-2}), but decreased V_{OC} (0.650±0.004 V vs. 0.695±0.004 V) and fill factor (*FF* = 0.67±0.01 vs. 0.70±0.01). The higher J_{SC} is due to absorption deeper into the NIR for TT-FIC. However, the increased LUMO energy of TT-FIC and decreased blend crystallization results in the lower V_{OC} and *FF*. In contrast to the PCE-10:BT-CIC binary cell, the incorporation of TT-FIC into the PCE-10:BT-CIC blend significantly increases J_{SC}, without changes to V_{OC} and *FF*. The trend in the performance of the ternary cells vs. acceptor blending ratio are shown in **Figure 2b**. The optimized devices comprised 1:1.25:0.5 PCE-10:BT-CIC:TT-FIC, with *PCE* = 12.6±0.3%, V_{OC} = 0.693±0.005 V, J_{SC} = 25.5±0.4 mA cm^{-2}, and *FF* = 0.71±0.1. This is more than a 15% enhancement in *PCE* compared with the reference cell. We also note that this efficiency is among the highest value reported for ternary blend OPVs so far. **Figure 2c** shows a *PCE* histogram for a population of 50 devices. The efficiencies fall in a narrow range between 12.0% and 12.6% with the mean value of 12.4%.

The external quantum efficiencies (*EQE*) vs. wavelength are shown in **Figure 2d** for several different tenary blend ratios. Increasing the TT-FIC content gradually increases *EQE* at long wavelengths. The integrated photocurrents from the *EQE* spectra are consistent with

This article is protected by copyright. All rights reserved.

Author Manuscript

the J_{SC} values obtained using the solar simulator (see **Table 1**), confirming the high photocurrent generation efficiency in the ternary devices. Importantly, the *EQE* of the PCE-10:BT-CIC:TT-FIC (1:1.25:0.5, 95 nm) cell reaches 75%, between λ= 650 nm and 900 nm, while leaving a transparency window at λ < 600 nm. This makes this device suitable for use as the back subcell (i.e. the cell adjacent to the reflective cathode) in a series-connected tandem OPV.

A DTDCPB:C_{70} (1:2, w/w) blend was chosen as the active region of the front subcell of the tandem due to its response in the wavelength range from 350 nm to 600 nm[23]. Therefore, DTDCPB:C_{70} and PCE-10:BT-CIC:TT-FIC sub-cells have complementary absorption spectra, as required in tandem solar cells. The tandem device structure is shown in **Figure 3a**, where the DTDCPB:C_{70} subcell grown by VTE, and the solution-processed PCE-10:BT-CIC:TT-FIC subcell was series connected with a charge recombination zone comprising bathophenanthroline (BPhen):C_{60} (8 nm)/Ag NP/PEDOT:PSS (50 nm). The BPhen:C_{60} serves as an exciton blocking layer[24], the PEDOT:PSS functions as both a hole transporting layer and a cap that protects the VTE-grown front subcell from penetration by the solution used in processing the back subcell. The 3 Å thick Ag nanoparticle layer promotes charge recombination[25]. The simulated relative absorbed power distribution is displayed in **Figure 3a**. The ternary back cell absorbs in the NIR from 700 nm to 950 nm, while the largest absorption occurs between λ= 350 nm and 700 nm in the front cell. The charge recombination zone is nearly optically lossless.

Figure 3b presents the *J–V* characteristics of the tandem cells, with details summarized in **Table 2**. As a result of insufficient light absorption by the DTDCPB:C_{70} front subcell that lacks a reflecting metal cathode, thicker films are required to balance currents between the subcells compared to previously reported 80 nm thick single-junction structures[23]. **Figure S4** shows the *J-V* characteristics of the tandem cells with various

This article is protected by copyright. All rights reserved.

Author Manuscript

DTDCPB:C_{70} thicknesses. The optimized tandem cell with 170 nm DTDCPB:C_{70} together with the 85 nm PCE-10:BT-CIC:TT-FIC back subcell exhibits J_{SC} = 13.3 ± 0.2 mA/cm^2, V_{OC} = 1.56 ± 0.01 V, *FF* = 0.71 ± 0.01 and *PCE* = 14.7 ± 0.3% measured with mask to eliminate edge effects[26, 27]. In contrast to our previous work[10] (see **Table 2**), the J_{SC} for this tandem OPV have been increased due to the red-shifted absorption of the ternary subcell. The performance of the 9 mm^2 tandem cells are found in Table 2, showing ~3% (relative) lower efficiency than the 2 mm^2 devices. We also note that the V_{OC} of the tandem equals the sum of the V_{OC} of the single junction cells from which it is comprised, indicating the lossless charge recombination by the Ag NPs.

Figure 3c shows a *PCE* histogram of a population of 32 optimized tandem devices. The efficiencies fall in a narrow range between 14.2% and 14.8%. An antireflection coating (ARC) layer consisting of a 120 nm MgF_2 (index of refraction, n_{MgF2} = 1.38 ± 0.01) and 130 nm SiO_2 deposited at glancing incidence to lower the refractive index to n_{SiO2} = 1.12 ± 0.03 was used to reduce optical losses and further increase the efficiency[28]. The reflection ratio of the glass substrate with and without the ARC decreases by ~ 4% between λ= 400 nm and 1000 nm (see **Figure S5)**. The ARC-coated tandem cell shows an increased J_{SC} from 13.3 ± 0.2 mA/cm^2 to 13.8 ± 0.3 mA/cm^2, thus leading to an increase in *PCE* = 15.4 ± 0.3%.

The *J–V* characteristics of tandem cells without ARC were also measured under incident light intensities varied from 12 to 100 mW cm^{-2} using neutral density filters, with results shown in **Figure S6**. The J_{SC} is proportional to light intensity, indicating a lack of space charge build-up within the two subcells and in the charge recombination zone. The *FF* of the tandem devices increased to 75% under low light intensity, which is due to reduced charge recombination. The *EQE* spectra of the single junction DTDCPB:C_{70} (1:2, 170 nm) and PCE-10:BT-CIC:TT-FIC (1:1.25:0.5, 85 nm) cells are plotted in **Figure 3d** (circles and

This article is protected by copyright. All rights reserved.

Author Manuscript

squares, respectively), as well as the individual sub-cells under illumination conditions experienced in the tandem cell.

Measuring the *EQE* for a tandem cell is significantly more challenging compared single junction solar cells[29, 30]. Here, we measure the *EQE* of the individual sub-cells using both an optical and electrical bias (see SI for details). As shown in **Figure 3d,** the subcells in the tandem architecture with the ARC absorb between λ = 350 and 1000 nm, both exhibiting a peak *EQE* ~ 75. The DTDCPB:C_{70} (1:2, 170 nm) cell in the tandem exhibits a reduced *EQE* at 400 < λ < 700 nm compared to the single junction cell at the same thickness due to residual absorption by the PCE-10:BT-CIC:TT-FIC cell. The integrated J_{SC} = 13.4 mA cm^{-2} for the front subcell and J_{SC} = 13.5 mA cm^{-2} for the black subcell, leading to balanced current generation in each subcell. Interestingly, the mathematically sum of the quantum efficiencies of the front and back subcells in the tandem features a nearly wavelength-independent quantum efficiency ~ 80% from λ = 400 to 1000 nm.

Ⅲ. DISCUSSION

The development of small energy gap materials is essential to the progress of OPV technology, although there exists trade-offs between E_g and E_{loss} that ultimately limits their performance[9]. Introducing a third NIR absorber into the active region appears to balance this limitation, since ternary systems benefit by improving both the J_{SC} through NIR absorption while reducing E_{loss}, thus increasing V_{OC}. In this work, the *Jsc* in the PCE-10:BT-CIC:TT-FIC ternary cell is significantly increased (from 22.3 mA cm^{-2} to 25.5 mA cm^{-2}), due to the increase in absorption between 600 and 1000 nm as TT-FIC is incorporated into the ternary blend. Additionally, the reduced phase separation in ternary blends increases the interfacial area between donors and acceptors, thus promoting exciton dissociation and giving rise to improved J_{SC}. Furthermore, the PCE-10:BT-CIC:TT-FIC based ternary cell shows a

This article is protected by copyright. All rights reserved.

Author Manuscript

decreased E_{loss} compared to the PCE-10:BT-CIC binary cell (from 0.64 to 0.55 eV). This small E_{loss} is possibly due to the decreased HOMO energy offset with the NFAs and PCE-10 compared to BT-CIC. Previous studies have shown that minimizing the offset energies leads to a reduction in E_{loss} [31-33].

Compared to the PCE-10:BT-CIC:TT-FIC (1:1.25:0.5, w/w/w) ternary cell, the TT-FIC-based binary device shows decreased J_{SC} (24.7±0.6 mA cm^{-2} vs. 25.5±0.4 mA cm^{-2}), V_{OC} (0.650±0.004 V vs. 0.693±0.005 V) and fill factor (*FF* = 0.67±0.01 vs. 0.71±0.01). For the series-connected multijunction devices, the voltage across the device is equal to the sum of the voltages across each subcell according to Kirchhoff's law. In other words, the increased V_{OC} of subcell obtained with the ternary device results in a higher V_{OC} in the tandem device. Moreover, the *FFs* of the tandem cells rely on the *FFs* of each subcell. Therefore, the higher *FF* of the ternary subcell further improves the performance of tandem. Based on these considerations, the efficiency of tandem device is further increased by using ternary vs. binary subcells.

The PCE-10:BT-CIC:TT-FIC ternary device can also achieve *EQE* = 75% between the wavelengths of λ = 650 nm and 900 nm, in addition to a transparency window between λ = 350 nm and 650 nm. The tandem OPV that comprises the VTE-deposited fullerene binary subcell and the solution-processed ternary NIR subcell shows a higher *PCE* = 15.4 ± 0.3% with obvious increases in J_{SC} compared to the reference cell[10]. The higher J_{SC} is attributed to the extended absorption of the ternary subcell. This suggests that the addition of ternary subcells with complementary absorption in tandem OPVs is a means for increasing *PCE*. Furthermore, a high *FF* = 0.71 was achieved in our tandem device. This high *FF* is attributed to the lower light intensity in ternary subcell, resulting in reduced current density and bimolecular recombination (see **Figure S7)**. Since submitting our paper, Meng *et. al* reported a double ternary junction tandem cell with 17.3% *PCE*[34]. An unexplained result is the higher

This article is protected by copyright. All rights reserved.

Author Manuscript

voltage of the tandem cell compared to the sum of the individual subcells, that could be due to several factors such as different light intensities used for the various measurements. Nevertheless, this result points to the benefits that can be achieved using ternary subcells, as demonstrated in this work

IV. CONCLUSION

In summary, we demonstrated a highly efficient NIR-absorbing ternary solar cell with a polymer donor (PCE-10) and two NIR-absorbing NFAs (BT-CIC and TT-FIC). The second NFA component in the ternary blend extends absorption across a broader spectral range, achieves improved film morphology, and ultimately reduces energy losses. The optimized PCE-10:BT-CIC:TT-FIC based single junction cell exhibits *PCE* = 12.6±0.3%. The tandem device structure incorporating a ternary NFA and a fullerene binary subcell shows *PCE* = 15.4±0.3%. This work points to a simple means for developing OPVs with very high efficiency, low E_{loss} NIR solar cells.

V. METHODS

Materials. All devices were grown on patterned indium tin oxide (ITO) substrates with sheet resistance of 15 Ω/ sq. The NIR absorbing-acceptor, BT-CIC and TT-FIC, were synthesized by our group. Other materials were purchased from commercial suppliers: MoO_3 (Acros Organics); DTDCPB, BPhen and TmPyPB (Luminescence Technology Corp.); C_{70} (SES Research); C_{60} (MER Corp.); PEDOT:PSS (Clevios P VP AI. 4083, Heraeus); PCE-10 (1-Material); Ag (Alfa Aesar). DTDCPB, C_{60} and C_{70} were purified once by temperature-gradient sublimation prior to deposition.

This article is protected by copyright. All rights reserved.

Author Manuscript

Single junction solar cell fabrication. Pre-patterned ITO on glass substrates were cleaned using a series of detergents and solvents followed by CO_2 snow cleaning and exposed to ultraviolet-ozone for 15 mins before growth[35]. The PEDOT:PSS was filtered once with a 0.45 μm Nylon syringe filter prior to use, and then spin-coated onto the substrate at 5000 rpm for 60 s. The active layer, PCE-10:BT-CIC:TT-FIC (1:*x*:*y* *w*/*w*/*w*), was dissolved in chlorobenzene:chloroform (CB:CF, 9:1 by vol.) with a concentration of 20 mg/ml. The solution was stirred overnight on a hot plate at 65°C, and then spin-coated at 2000 rpm for 90s to achieve a thickness of ~95 nm. The samples were then transferred back to the vacuum chamber for deposition of TmPyPB and the Ag cathode. For the PCE-10:TT-FIC based device, ZnO nanoparticles were used for an electron transporting layer. The device areas of 2.0 and 9.0 mm^2 were defined by the overlap between the patterned ITO and the Ag cathode deposited through an ultrathin shadow mask (50 μm).

Tandem solar cell fabrication. Pre-patterned ITO on glass substrates were cleaned using a series of detergents and solvents followed by CO_2 snow cleaning and exposed to ultraviolet-ozone for 15 mins before growth. The vacuum-deposited layers for the front cell were grown at ~ 1 Å/s in a high vacuum chamber with a base pressure of 2×10^{-7} torr. During co-deposition of the VTE-grown DTDCPB:C_{70} (1:2, w/w) layer, the deposition rate of each material is monitored by individual crystal sensors to achieve the desired volume ratios. After growing the active layer, a recombination zone consists of three layers: a 3 Å thick Ag NP layer deposited on the BPhen:C_{60} mixed (1:1, w/w), followed by spin-coating the PEDOT:PSS (Clevios P VP AI. 4083, Heraeus) was built up. The vacuum chamber is connected to glove boxes filled with ultrapure N_2 (O_2, H_2O < 0.1 ppm) where the solution processed layers were subsequently deposited. The back NIR cells were made according to the single junction procedure. The ARC was grown onto the glass substrate after the devices were complete. MgF_2 was deposited by VTE while the SiO_2 was grown by electron beam

This article is protected by copyright. All rights reserved.

Author Manuscript

deposition with the substrate at an angle of 85° to the beam direction to achieve a low refractive index of 1.1.

Solar cell characterization. The current density-voltage (*J-V*) characteristics and spectrally resolved external quantum efficiencies (*EQE*) were measured in a glove box filled with ultrapure N_2 (< 0.1 ppm). Light from a Xe lamp filtered to achieve a simulated AM 1.5G spectrum (ASTM G173-03) was used as the source for *J-V* measurements. The lamp intensity controlled by neutral density filters was calibrated using a standard Si reference cell (with a KG-2 filter) traceable to certification by National Renewable Energy Laboratory (NREL). The illumination intensity was adjusted using neutral density filters. Each cell was measured under six different light intensities from 0.001 sun to 1 sun (100 mW/cm^2). Errors quoted account for variations from three or more cells measured, as well as an additional systematic error of 5% for J_{SC} and *PCE*. The devices were masked with a metal aperture to define the active area of 0.012 ± 0.001 and 0.063 ± 0.001 cm^{-2} and measured in a light-tight sample holder to minimize edge effects. This ensured that both the reference and test cells were co-located under the solar simulator during measurement. The *EQE* measurements were performed with devices underfilled by a 200 Hz-chopped monochromated and focused beam from a Xe lamp. The current outputs from the devices as well as from a reference NIST-traceable Si detector were recorded using a lock-in amplifier. The *EQE* of the individual sub-cells in the tandem devices were measured by using both an optical and electrical bias. There is a ~2% difference between the integrated J_{SC} from light bias *EQE* measurements to that using the solar simulator with a mask. The details can be found in SI.

Competing interests

The authors declare no competing interests.

This article is protected by copyright. All rights reserved.

Author Manuscript

ACKNOWLEDGMENTS

YL and SRF were funded in part by the Office of Energy Efficiency and Renewable Energy (EERE), U.S. Department of Energy, under Award Number DE-EE0006708 and by the Department of the Navy, Office of Naval Research under Award No. N00014-17-1-2211. This work was also supported by the National Natural Science Foundation of China (51873139).

TABLES

Table 1. Operating characteristics of OPVs under simulated of AM 1.5G, 100 mW cm^{-2}, illumination.

PCE-10:BT-CIC:TT-FIC	J_{sc} [a] [mA/cm^2]	V_{oc} [V]	*FF*	*PCE* [b] [%]
1:1.5:0	22.3±0.4 (21.2)	0.695±0.004	0.70 ± 0.01	10.8±0.2
1:1.25:0.25	23.8±0.4 (23.3)	0.696±0.005	0.71 ± 0.01	11.7±0.2
1:1.25:0.5	25.5±0.3 (24.4)	0.693±0.005	0.71 ± 0.01	12.6±0.3
1:1.25:0.75	26.6±0.4 (24.9)	0.687±0.006	0.66 ± 0.01	12.1±0.3
1:0:1.5	24.7± 0.6 (23.8)	0.650±0.004	0.67 ± 0.01	10.8±0.2

[a] The values in parentheses are calculated from the integral of the *EQE* spectrum.
[b] The average value is based on measurement of 50 devices.

Table 2. Discrete subcell and tandem device performances.

Device	***J_{SC} (mA/cm^2)***	***V_{OC} (V)***	***FF***	***PCE (%)***

This article is protected by copyright. All rights reserved.

Author Manuscript

[Back] PCE-10:BT-CIC:TT-FIC (1:1.25:0.5, 85nm)	24.8 ± 0.3	0.69 ± 0.01	0.70 ± 0.01	12.4 ± 0.2
[Front] DTDCPB:C_{70} (1:2, 170nm)	17.1 ± 0.3	0.90 ± 0.01	0.65 ± 0.01	10.0 ± 0.2
[Tandem] (w/ternary NIR subcells, 2mm^2) [a]	13.3 ± 0.2 (13.0)[c]	1.56 ± 0.01	0.71 ± 0.01	14.7 ± 0.3
[Tandem] (w/binary NIR subcells, 2mm^2) [b]	12.7 ± 0.2	1.59 ± 0.01	0.71 ± 0.01	14.3 ± 0.3
[Tandem] (w/ternary NIR subcells, 9mm^2) [a]	12.8 ± 0.3 (12.6)[c]	1.56 ± 0.01	0.71 ± 0.01	14.2 ± 0.3
[Tandem] (ternary cells + ARC, 2mm^2) [a]	13.8 ± 0.3 (13.5)[c]	1.56 ± 0.01	0.71 ± 0.01	15.4 ± 0.3

[a] The J_{SC} values are measured from devices using masks, The details of the measurements are found in Methods.

[b] The data from ref. 4. J_{SC} values are measured from the devices without masks.

[c] The values in parentheses are calculated from the integral of the *EQE* spectrum using light bias with electrical bias corrected. The details of the measurement are found in Methods and Supplementary Information (SI).

Author Manuscript

REFERENCES

[1] B. Qu, S. R. Forrest, *Appl. Phys. Lett.* **2018**, *113*, 053302.

[2] J. Y. Kim, K. Lee, N. E. Coates, D. Moses, T.-Q. Nguyen, M. Dante, A. J. Heeger, *Science* **2007**, *317*, 222-225.

[3] A. Hadipour, B. de Boer, J. Wildeman, F. B. Kooistra, J. C. Hummelen, M. G. Turbiez, M. M. Wienk, R. A. Janssen, P. W. Blom, *Adv. Funct. Mater.* **2006**, *16*, 1897-1903.

[4] J. Gilot, M. M. Wienk, R. A. J. Janssen, *Adv. Mater.* **2010**, *22*, E67-E71.

[5] X. Che, X. Xiao, J. D. Zimmerman, D. Fan, S. R. Forrest, *Adv. Energy Mater.* **2014**, *4*, 1400568.

[6] L. Dou, J. You, J. Yang, C.-C. Chen, Y. He, S. Murase, T. Moriarty, K. Emery, G. Li, Y. Yang, *Nature Photon.* **2012**, *6*, 180-185.

[7] L. Dou, Y. Liu, Z. Hong, G. Li, Y. Yang, *Chem. Rev.* **2015**, *115*, 12633-12665.

This article is protected by copyright. All rights reserved.

[8] Y. Li, J. Zou, H.-L. Yip, C.-Z. Li, Y. Zhang, C.-C. Chueh, J. Intemann, Y. Xu, P.-W. Liang, Y. Chen, A. K. Y. Jen, *Macromolecules* **2013**, *46*, 5497-5503.

[9] Y. Li, L. Zhong, B. Gautam, H.-J. Bin, J.-D. Lin, F.-P. Wu, Z. Zhang, Z.-Q. Jiang, Z.-G. Zhang, K. Gundogdu, Y. Li, L.-S. Liao, *Energy Environ. Sci.* **2017**, *10*, 1610-1620.

[10] X. Z. Che, Y. X. Li, Y. Qu, S. R. Forrest, *Nature Energy* **2018**, *3*, 422-427.

[11] Y. Li, J.-D. Lin, X. Che, Y. Qu, F. Liu, L.-S. Liao, S. R. Forrest, *J. Am. Chem. Soc.* **2017**, *139*, 17114-17119.

[12] H. Yao, Y. Cui, R. Yu, B. Gao, H. Zhang, J. Hou, *Angew. Chem. Int. Edit.* **2017**, *56*, 3045-3049.

[13] Z. Yao, X. Liao, K. Gao, F. Lin, X. Xu, X. Shi, L. Zuo, F. Liu, Y. Chen, A. K. Y. Jen, *J. Am. Chem. Soc.* **2018**, *140*, 2054-2057.

[14] S. Dai, T. Li, W. Wang, Y. Xiao, T. K. Lau, Z. Li, K. Liu, X. Lu, X. Zhan, *Adv. Mater.* **2018**, *30*, 1706571.

[15] F. Liu, Z. Zhou, C. Zhang, J. Zhang, Q. Hu, T. Vergote, F. Liu, T. P. Russell, X. Zhu, *Adv. Mater.* **2017**, *29*, 1606574.

[16] Z. Xiao, X. Jia, D. Li, S. Wang, X. Geng, F. Liu, J. Chen, S. Yang, T. P. Russell, L. Ding, *Sci. Bull.* **2017**, *62*, 1494-1496.

[17] L. Lu, M. A. Kelly, W. You, L. Yu, *Nature Photon.* **2015**, *9*, 491.

[18] Q. An, F. Zhang, J. Zhang, W. Tang, Z. Deng, B. Hu, *Energy Environ. Sci.* **2016**, *9*, 281-322.

[19] H. Fu, Z. Wang, Y. Sun, *Solar RRL* **2018**, *2*, 1700158.

[20] T. Liu, Y. Guo, Y. Yi, L. Hou, X. Xue, X. Sun, H. Fu, W. Xiong, D. Meng, Z. Wang, F. Liu, T. Russell, Y. Sun, *Adv. Mater.* **2016**, *28*, 10008-10015.

[21] R. Yu, S. Zhang, H. Yao, B. Guo, S. Li, H, Zhang, M. Zhang, J, Hou, *Adv. Mater.* **2017**, *29*, 1700437.

[22] D. Baran, R. S. Ashraf, D. A. Hanifi, M. Abdelsamie, N. Gasparini, J. A. Rohr, S. Holliday, A. Wadsworth, S. Lockett, M. Neophytou, C. J. Emmott, J. Nelson, C. J. Brabec, A. Amassian, A. Salleo, T. Kirchartz, J. R. Durrant, I. McCulloch, *Nat. Mater.* **2017**, 16, 363-369.

[23] O. L. Griffith, X. Liu, J. A. Amonoo, P. I. Djurovich, M. E. Thompson, P. F. Green, S. R. Forrest, *Phys. Rev. B* **2015**, *92*, 085404.

[24] A. N. Bartynski, C. Trinh, A. Panda, K. Bergemann, B. E. Lassiter, J. D. Zimmerman, S. R. Forrest, M. E. Thompson, *Nano Lett.* **2013**, *13*, 3315-3320.

This article is protected by copyright. All rights reserved.

Author Manuscript

[25] A. Yakimov, S. R. Forrest, *Appl. Phys. Lett.* **2002**, *80*, 1667-1669.

[26] H. J. Snaith, *Energy Environ. Sci.* **2012**, *5*, 6513-6520.

[27] Q. Burlingame, C. Coburn, X. Che, A. Panda, Y. Qu, S. R. Forrest, *Nature* **2018**, *554*, 77.

[28] J. Q. Xi, J. K. Kim, E. F. Schubert, D. Ye, T. M. Lu, S.-Y. Lin, J. S. Juneja, *Opt. Lett.* **2006**, *31*, 601-603.

[29] J. Gilot, M. M. Wienk, R. A. J. Janssen, *Adv. Funct. Mater.* **2010**, *20*, 3904-3911.

[30] W. Li, A. Furlan, K. H. Hendriks, M. M. Wienk, R. A. J. Janssen, *J. Am. Chem. Soc.* **2013**, *135*, 5529-5532.

[31] W. Li, K. H. Hendriks, A. Furlan, M. M. Wienk, R. A. J. Janssen, *J. Am. Chem. Soc.* **2015**, *137*, 2231-2234.

[32] K. Vandewal, Z. Ma, J. Bergqvist, Z. Tang, E. Wang, P. Henriksson, K. Tvingstedt, M. R. Andersson, F. Zhang, O. Inganäs, *Adv. Funct. Mater.* **2012**, *22*, 3480-3490.

[33] Y. Li, X. Liu, F.-P. Wu, Y. Zhou, Z.-Q. Jiang, B. Song, Y. Xia, Z.-G. Zhang, F. Gao, O. Inganas, Y. Li, L.-S. Liao, *J. Mater. Chem. A* **2016**, *4*, 5890-5897.

[34] L. Meng, Y. Zhang, X. Wan, C. Li, X. Zhang, Y. Wang, X. Ke, Z. Xiao, L. Ding, R. Xia, H. L. Yip, Y. Cao, Y. Cheng, *Science* **2018**, DOI: 10.1126/science.aat2612.

[35] N. Wang, X. Tong, Q. Burlingame, J. Yu, S. R. Forrest, *Sol. Energy Mater. and Sol. Cells* **2014**, *125*, 170-175.

FIGURE CAPTIONS

Figure 1. (a) Molecular structural formulae of PCE-10, BT-CIC and TT-FIC used in the single junction and tandem cells. (b) UV-Vis absorption spectra of PCE-10, BT-CIC and TT-FIC thin films.

Author Manuscript

This article is protected by copyright. All rights reserved.

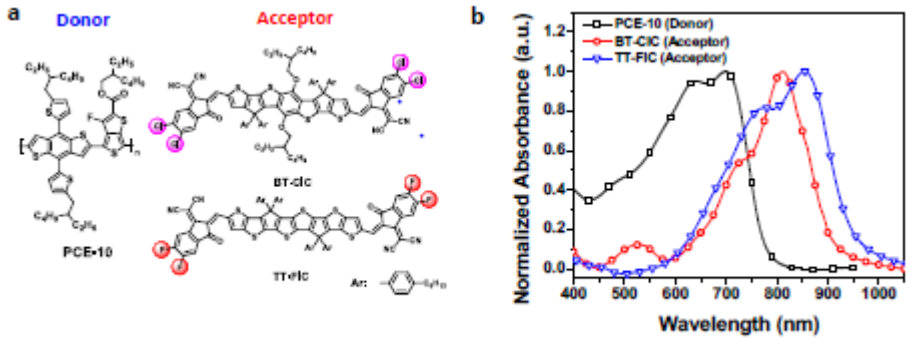

Figure 2. (a) UV-Vis absorption spectra of ternary blend films. (b) Energy level diagram of PCE-10, BT-CIC and TT-FIC relative to vacuum obtained from cyclic voltammetry. Numbers are in eV relative tot he vacuum level.

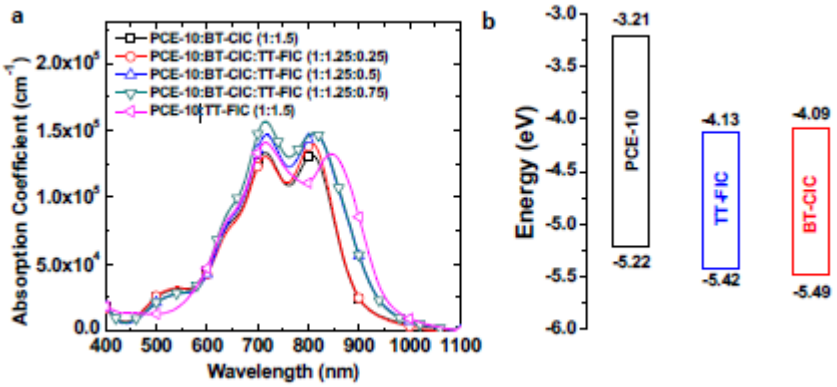

Figure 3. (a) Current-density-voltage characteristics of ternary cells based on PCE-10, BT-CIC and TT-FIC. (b) V_{OC}, J_{SC}, *FF* and *PCE* of optimized ternary cells as functions of TT-FIC:BT-CIC blend ratios, under 1 sun intensity (100 mW/cm^2), AM 1.5G simulated illumination.

Author Manuscript

This article is protected by copyright. All rights reserved.

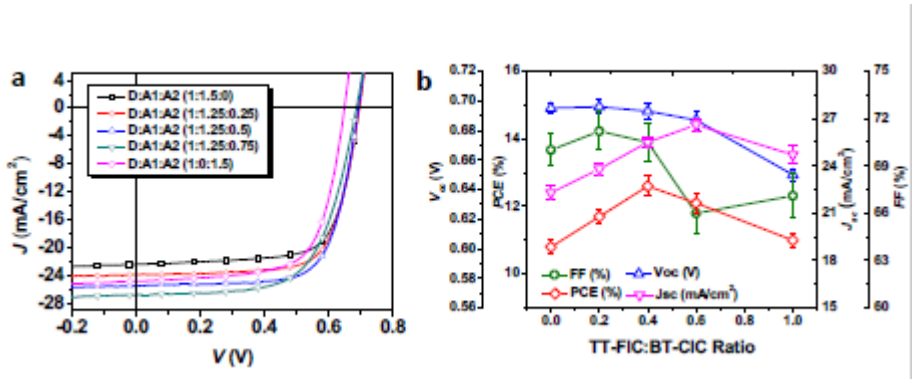

Figure 4. (a) Efficiency histogram for a population of 50 optimized ternary cells, and (b) external quantum efficiency (*EQE*) spectra of ternary cells with various blending ratios.

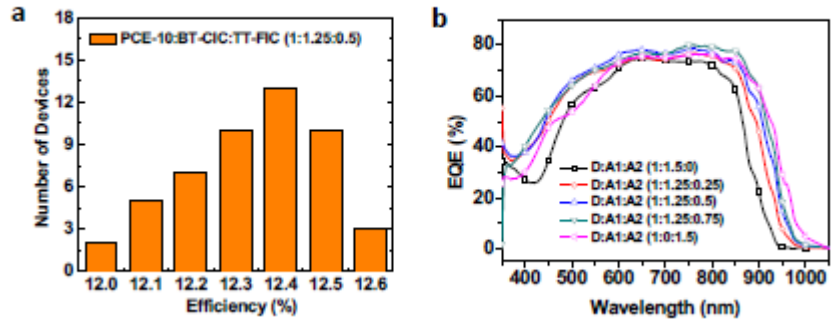

Figure 5. (a) Schematic of the tandem device showing optimized layer thicknesses and compositions. Also shown is the optical field intensity distribution within the cell obtained via the transfer matrix method. Note the non-overlapping spectra in the front (near the ITO) and back sub-cells leading to good current balance. (b) Current-density-voltage characteristics of the optimized tandem cell together with the single junction subcells. (c) Efficiency histogram for a population of 32 optimized tandem cells (2 mm^2 effective area, without antireflection coatings), and (d) external quantum efficiency (*EQE*) spectra of the tandem and discrete subcells. The symbols are for the discrete single junctions, while the magenta and blue lines are for the subcells in the stack obtained under light bias at wavelengths of 780 and 365 nm, and electrical bias of 0.45 and 0.75 V. The red line is the sum of the two measured *EQE*s obtained using light bias.

This article is protected by copyright. All rights reserved.

Author Manuscript

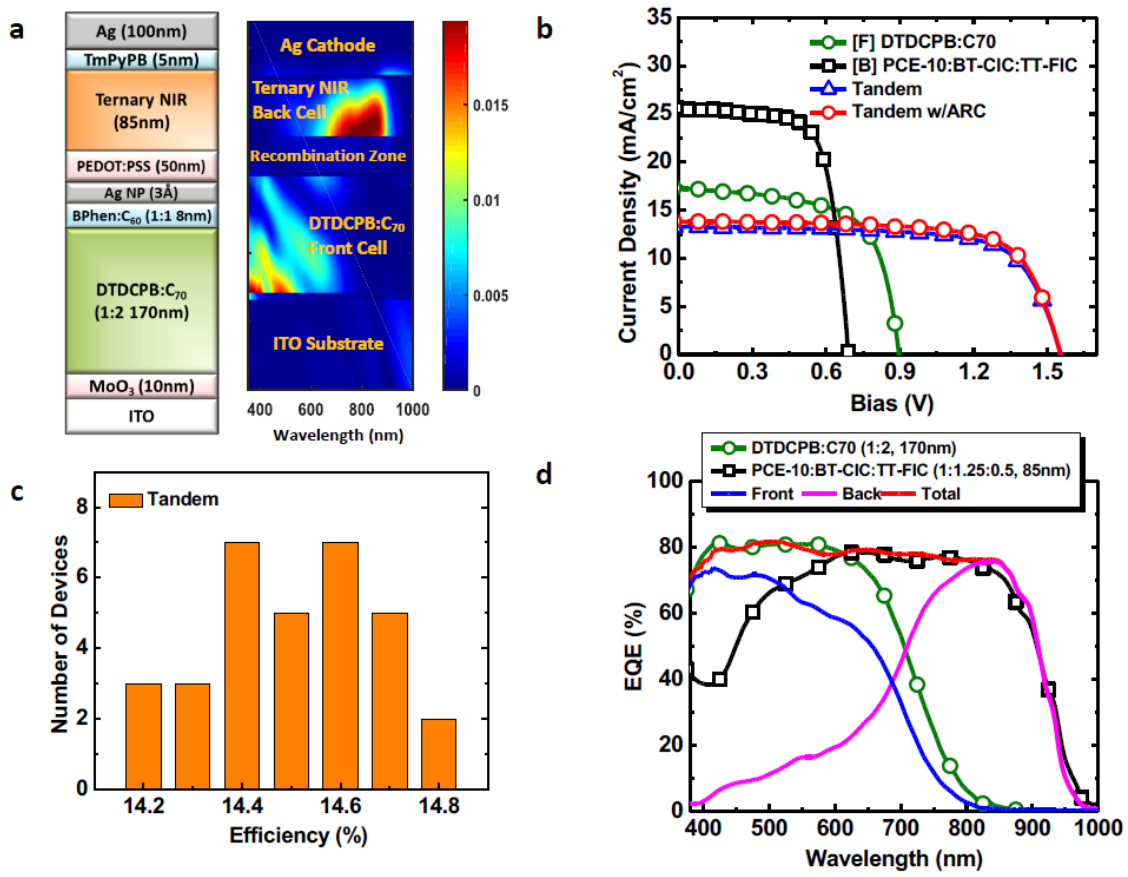

We report a tandem organic photovoltaic cell combining a non-fullerene acceptor-based ternary cell with a fullerene small molecule binary subcell. The cell combines vacuum and solution deposited layers, achieving a power conversion efficiency of 15.4%.

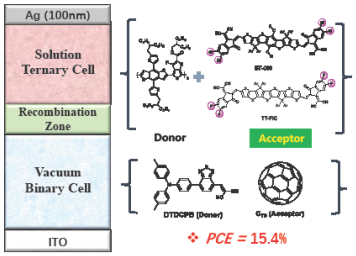

This article is protected by copyright. All rights reserved.